

## Modeling Seismic Attributes of $P_n$ Waves using the Spectral-Element Method

ALI C. BAKIR<sup>1</sup> and ROBERT L. NOWACK<sup>1</sup>

**Abstract**—To investigate the nature of  $P_n$  propagation, we have implemented the spectral-element method (SEM) for vertically and laterally varying media with and without attenuation. As a practical measure, essential features of the  $P_n$  waves are distilled into seismic attributes including arrival times, amplitudes and pulse frequencies. To validate the SEM simulations, we first compare the SEM results with reflectivity calculations of BRAILE and SMITH (Geophys. J.R. Astr. Soc. 40, 145–176, 1975) and then to the asymptotic results of ČERVENÝ and RAVINDRA (Theory of Seismic Headwaves, University of Toronto Press, pp. 235–250, 1971). Models with random, laterally varying Moho structures are then simulated, where the amplitude and pulse frequency characteristics are found to be stable to small Moho interface perturbations. SEM calculations for models with different upper-mantle velocity gradients are next performed where it is found that interference effects can strongly influence the  $P_n$  amplitudes and pulses frequencies. For larger-scale, laterally varying structures, SEM models similar to that found along the Hi-CLIMB array in Tibet are then performed. It is observed that large-scale structures, along with small-scale structures, upper-mantle velocity gradients and attenuation, can all significantly affect the  $P_n$  attributes. Ambiguities between upper-mantle velocity gradients and attenuation are also found when using  $P_n$  amplitudes and pulse frequency attributes. These ambiguities may be resolved, to some degree, by using the curvature of the travel times at longer regional distance, however, this would also be complicated by lateral variability.

**Key words:** Seismic  $P_n$  Waves, seismic attributes, spectral-element method.

### 1. Introduction

Head-waves are important seismic phases since they are the first arriving phases at long offsets. When a positive upper-mantle velocity gradient occurs, the head-wave or  $P_n$  phase is composed of a complex set of interfering waves (ČERVENÝ and RAVINDRA (1971; HILL, 1971; MENKE and RICHARDS, 1980). These

interfering waves can also simply result from the spherical nature of the Earth (HILL, 1973; SERENO and GIVEN, 1990, YANG *et al.*, 2007), which gives an effect equivalent to a velocity gradient in a corresponding flattened earth model. Amplitude variations of refracted waves with distance support the interpretation that these arrivals are composed of diving and interference waves, in contrast to pure head-waves (BRAILE and SMITH, 1975).

To account for the intricate nature of  $P_n$  propagation, we have implemented the spectral-element method (SEM) (KOMATITSCH and VILOTTE, 1998; KOMATITSCH *et al.*, 2005). The SEM approach can be applied in 2D or 3D and implemented in parallel using a message passing interface (MPI) library on large-cluster computing. Here we have applied a parallel 2D viscoelastic SEM code. As a practical measure, essential features of  $P_n$  waveforms are distilled into seismic attributes, including arrival times, envelopes of wave amplitudes, and pulse frequencies for modeling using the approach of MATHENEY and NOWACK (1995).

In order to validate the spectral-element method, wide-angle seismic results obtained using SEM are compared with the reflectivity results of BRAILE and SMITH (1975), and with the asymptotic results of ČERVENÝ and RAVINDRA (1971). For these comparisons, in addition to synthetic seismograms, various seismic attributes of the  $P_n$  are derived, including envelope amplitudes and pulse frequencies.

There has been a recent debate on the effects of geometric spreading from structural effects of the medium and intrinsic and scattering attenuation (MOROZOV, 2008, 2010; XIE, 2010). Here we investigate the effects of structural models on the amplitude and frequency characteristics of  $P_n$  waves. We first use the SEM approach to investigate models with randomly varying Moho structures to test the stability

<sup>1</sup> Department of Earth and Atmospheric Sciences, Purdue University, West Lafayette, IN 47907, USA. E-mail: alicanbakir@gmail.com; nowack@purdue.edu

of the results to small Moho changes in the model. SEM simulations for models with different upper-mantle velocity gradients are then performed, and results of the runs show that the  $Pn$  seismic attributes are strongly affected by the velocity gradients in the upper mantle. For larger-scale, laterally varying structures, we perform SEM simulations for structures similar to those found along the Hi-CLIMB array in Tibet with a ramp structure at the Moho by GRIFFIN *et al.* (2011), NÁBĚLEK *et al.* (2009), NOWACK *et al.* (2010) and TSENG *et al.* (2009). It is found that the large-scale structure can also significantly affect the  $Pn$  seismic attributes. However, ambiguities between upper-mantle velocity gradients and attenuation are found when using  $Pn$  amplitudes and pulse frequencies, which can possibly be resolved using the curvature of the travel times at longer regional distances.

## 2. Validation of the Spectral-Element Method for $Pn$ Waves

In order to validate the spectral-element method, comparisons are made between wide-angle SEM results and the reflectivity calculations of BRAILE and SMITH (1975), as well as between the SEM results and the asymptotic results of ČERVENÝ and RAVINDRA (1971). For these comparisons, in addition to the synthetic seismograms, various seismic attributes of the  $Pn$  are derived, including travel times, pulse amplitudes and pulse frequencies. The SEM calculations are implemented using the parallel code SPECFEM2D (KOMATITSCH and VILOTTE, 1998; KOMATITSCH *et al.*, 2005).

We first compare the SEM with the reflectivity calculations. For various wide-angle applications, the reflectivity method has been extensively used to compute synthetic seismograms in vertically varying media. For example, BRAILE and SMITH (1975) computed synthetic seismograms using the reflectivity method and examined the effects of various velocity-depth models on the calculated seismic waves. The first comparison is for a model with a constant velocity 30 km crust over a constant velocity mantle, and is called Moho-1 by BRAILE and SMITH (1975). The P-wave velocity in the crust is 6.4 km/s and in

the mantle is 8.0 km/s. The S-wave velocities are computed assuming a Poisson solid, and the densities are computed from the P-wave velocities using Birch's law (BRAILE and SMITH, 1975). As described in the Appendix A, the initial pulses used in the two modeling techniques first need to be matched, and also an approximate 2D to 3D correction needs to be applied to the SEM calculations. In Fig. 1a, the results of BRAILE and SMITH (1975) for model Moho-1 (solid line) are shown and the results of the SEM (dashed line) are superposed. Both results are multiplied by distance for plotting purposes. As can be seen from the comparison, a good agreement is found. Since there is no upper-mantle velocity gradient for this case, the amplitudes of the  $Pn$  arrivals are small compared to the  $PmP$  arrivals.

The second comparison with reflectivity results is performed using a constant velocity 30 km crust over a positive velocity gradient in the top 5 km of the mantle, and is called Moho-5 by BRAILE and SMITH (1975). The P-wave velocity of the crust is 6.4 km/s. A velocity gradient in the upper-mantle for 5 km below the Moho is given by  $\alpha_2(z) = \alpha_2^{\text{top}} + bz$ , where  $\alpha_2^{\text{top}}$  is the top velocity of the mantle of 8 km/s,  $b$  is the velocity gradient of  $0.08 \text{ s}^{-1}$ , and  $z$  is the depth below the Moho. At the depth of 35 km, the velocity of the mantle is 8.4 km/s down to the bottom of the model at 60 km in depth. The computation of the S-wave velocities and densities is done in a similar manner as the first case given above. The comparisons between the reflectivity the SEM results are shown in Fig. 1b and are in a good agreement. For the zone around the critical distance at 80 km, larger amplitude arrivals occur resulting from the onset of the wide-angle reflected waves and the initiation of the head-waves. The size of this zone depends on the frequency content of the source where lower frequencies will cause a larger interference zone (BRAILE and SMITH, 1975).

Comparing Fig. 1a and b, the  $Pn$  amplitudes for the second model are much larger than those of the first model. This is due to the presence of a positive velocity gradient below the Moho for the second model (HILL, 1971). The resulting interference head-waves have a similar initial travel time onset as the pure head-waves, but then begin to curve for increasing distance due to the upper-mantle velocity

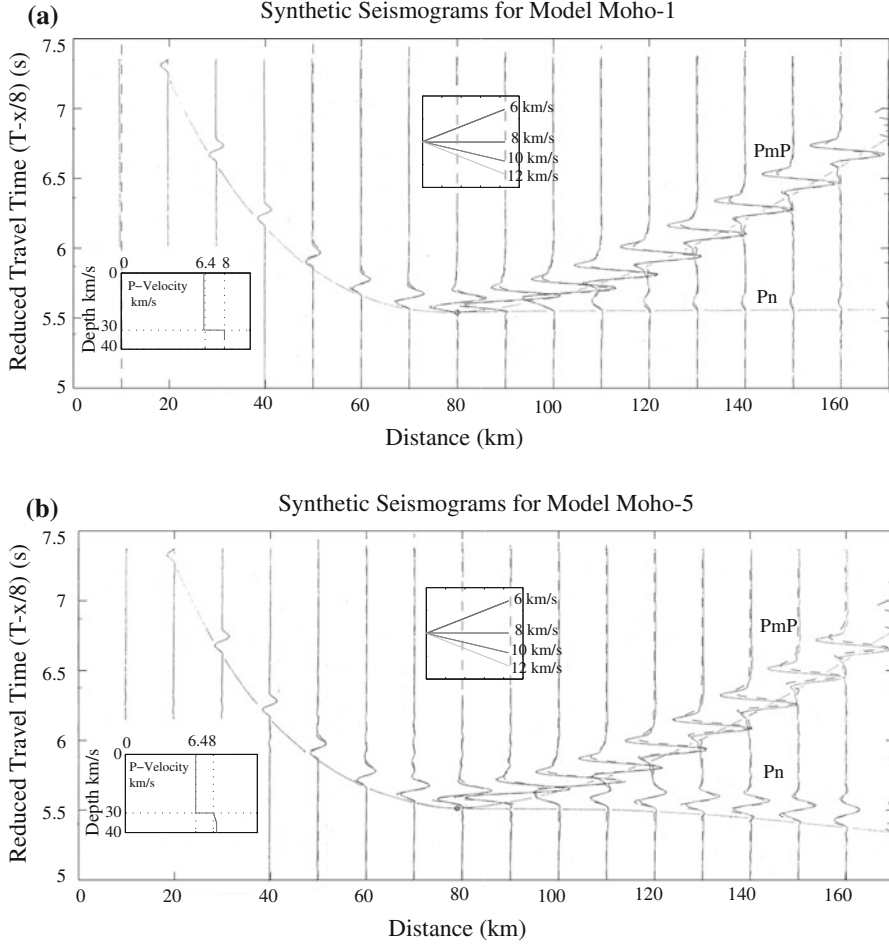


Figure 1

**a** A comparison between the SEM calculations (*dashed*) and the reflectivity results (*solid*) of BRAILE and SMITH (1975) for a model with a constant velocity 30 km crust over a constant velocity mantle. The amplitudes of the reflectivity results and the 3D corrected SEM results are both multiplied by distance in the plot. **b** A comparison between the results from the SEM calculations (*dashed*) and the reflectivity results (*solid*) of BRAILE and SMITH (1975) for a constant velocity 30 km crust over a mantle with a velocity gradient in the top 5 km. Amplitudes of the reflectivity results and the corrected SEM results are both multiplied by distance in the plot

gradient. The amplitude characteristics of interference head-waves are also very different from the pure head-waves (BRAILE and SMITH, 1975).

SEM results are next compared with the asymptotic results of ČERVENÝ and RAVINDRA (1971). The pure head-wave case has a constant velocity 30 km crust over a constant velocity mantle model, where the P-wave velocity in the crust is 6.4 km/s and in the mantle is 8 km/s. ČERVENÝ and RAVINDRA (1971) specify the densities of the crust and mantle to be the same with  $\rho_1/\rho_2 = 1$ . The interference head-wave case of ČERVENÝ and RAVINDRA (1971) has a constant velocity

30 km crust over a positive velocity gradient mantle. The velocity in the lower medium is given by  $\alpha_2(z) = \alpha_2^{\text{top}} + bz$  where  $\alpha_2^{\text{top}}$  is the top velocity of the mantle equal to 8 km/s,  $b$  is the velocity gradient equal to 0.02264 1/s and  $z$  is the depth below the Moho.

Figure 2a shows a comparison between the amplitudes for the pure and interference head-waves for the asymptotic results of ČERVENÝ and RAVINDRA (1971) (background plot) and the SEM results (crosses) superposed. For the background plot of ČERVENÝ and RAVINDRA (1971),  $C^+$  is the interference head wave amplitude, 131 is the pure head wave, II is

the reflected wave amplitude, and  $r_{131}^*$  is the critical distance for the pure head-wave. Because the amplitude variations with distance are different for the 3D asymptotics and 2D SEM (CHEW, 1990), approximate 2D to 3D corrections given in Appendix A have been applied to the SEM calculations. As seen in Fig. 2a, there is a good agreement between the asymptotic calculations of ČERVENÝ and RAVINDRA (1971) and the SEM results for the pure and interference head-wave cases. Again, the existence of a positive upper-mantle velocity gradient drastically increases the head-wave amplitudes (ČERVENÝ and RAVINDRA, 1971).

The incident and  $Pn$  pulse amplitude spectra as a function of distance are given in Fig. 2b, where the initial pulse has a dominant frequency of 6.4 Hz. At the onset distance of the  $Pn$  wave, the centroid frequency of the  $Pn$  pulse spectra at 140 km is lower

than that of the incident wave. The centroid frequency then starts increasing and becoming larger than that of the incident wave at 180 km resulting from tuning effects between the different interference waves. For greater distances, the diving waves begin to dominate, and this causes a lowering of the centroid frequency approaching that of the incident wave. This behavior is consistent with the reflectivity and asymptotic Gaussian beam calculations of NOWACK and STACY (2002).

### 3. SEM Simulations for Laterally Varying Moho Depths

Several SEM simulations are next performed for models with randomly varying Moho depths. For each random Moho depth model, a Gaussian pseudo-

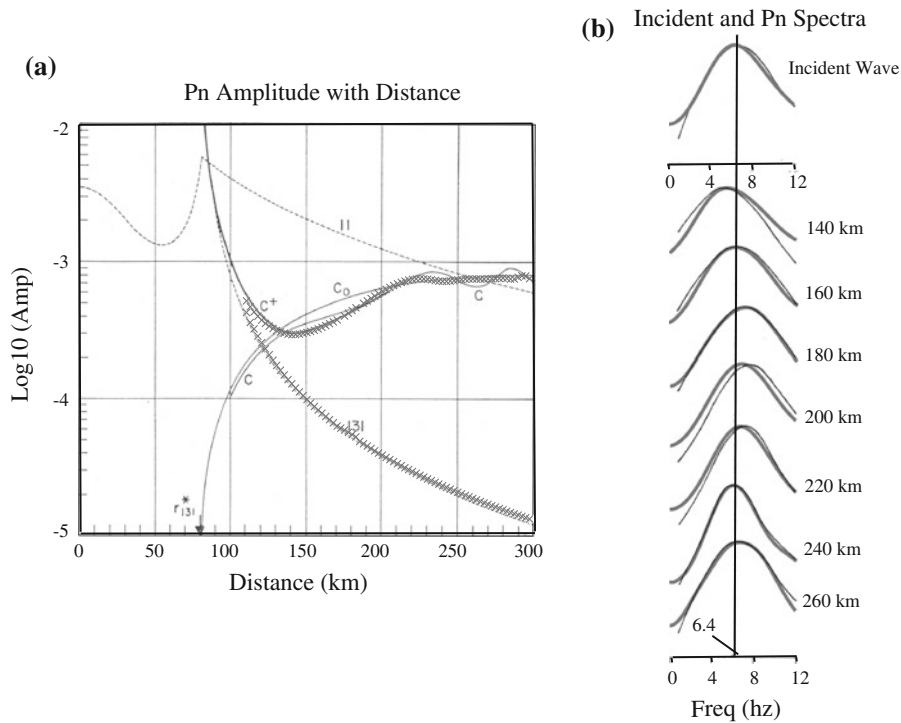


Figure 2

**a** A comparison between the SEM amplitude calculations (crosses) and the asymptotic results (background plot modified from ČERVENÝ and RAVINDRA, 1971) for the pure and interference head-waves. For the background plot,  $C^+$  is the interference head-wave amplitude, the  $C_0$  is the diving wave amplitude, the 131 wave is the pure head-wave case, II is the reflected wave amplitude, and  $r_{131}^*$  is the critical distance for the pure head-wave. The SEM simulations are corrected from 2D to 3D as in Appendix A. **b** This shows the amplitude spectra as a function of distance for the interference head-wave. The thin black curves are from ČERVENÝ and RAVINDRA (1971) and the thick black curves are from the SEM calculations

random number generator is used to generate Moho depths with the parameters given by the standard deviation, a mean depth of 30 km, and a 1 km horizontal sampling. A smoothing window is then applied to the results. The first model has a standard deviation of 0.1 km in depth and a horizontal smoothing length of 20 km, and second model has a standard deviation of 0.25 km in depth and a horizontal smoothing length of 40 km. Figure 3 (top) shows two randomly generated Moho depths for the first model, where two different realizations are labeled as “A” and “B”. The bottom plot in Fig. 3 is shown to illustrate how the variations of the interfaces would look at a more geologic scale. Except for the interface parameters (standard deviation and smoothing length), the other model parameters, including the upper mantle velocity gradient, are the same as that used for interference head-wave case shown in Fig. 2.

The SEM amplitudes for the first randomly varying Moho models are given in Fig. 4a, and are compared with the interference head-wave results for the reference model from ČERVENÝ and RAVINDRA

(1971). The SEM simulations are corrected from 2D to 3D as in Appendix A. It can be seen that the amplitudes of the two realizations for the first random Moho depth models vary about the background amplitude curves indicating that small interface perturbations affect the amplitudes in a stable fashion. For the same standard deviation and horizontal smoothing length, the A and B realizations for the first random Moho model have a very similar range of amplitudes about the background amplitude curve. Figure 4b displays the pulse spectra for the A realizations for the first model showing that the pulse frequencies are stable compared to the background model results for small perturbations in Moho depth.

Figure 5 (top) shows two randomly generated Moho depths for the second model which has a standard deviation of 0.25 km in depth and a horizontal smoothing length of 40 km. Two different realizations for the same parameters are again labeled as “A” and “B”. The bottom plot in Fig. 5 is shown to illustrate how the variations of the interfaces would look at a more geologic scale. Except for the interface

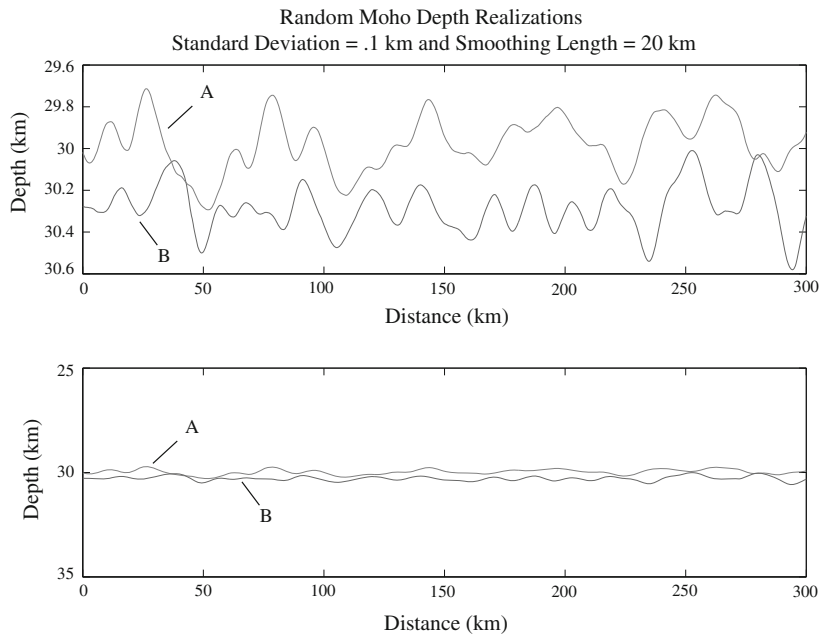


Figure 3

This shows two realizations of random Moho depths A and B for models with a standard deviation of 0.1 km in depth and a horizontal smoothing length of 20 km in distance. The upper mantle velocity gradient is the same as that used in Fig. 2. Both realizations are centered at 30 km and slightly shifted for plotting purposes. The top plot shows a zoomed view of the interfaces, and the bottom plot is less magnified

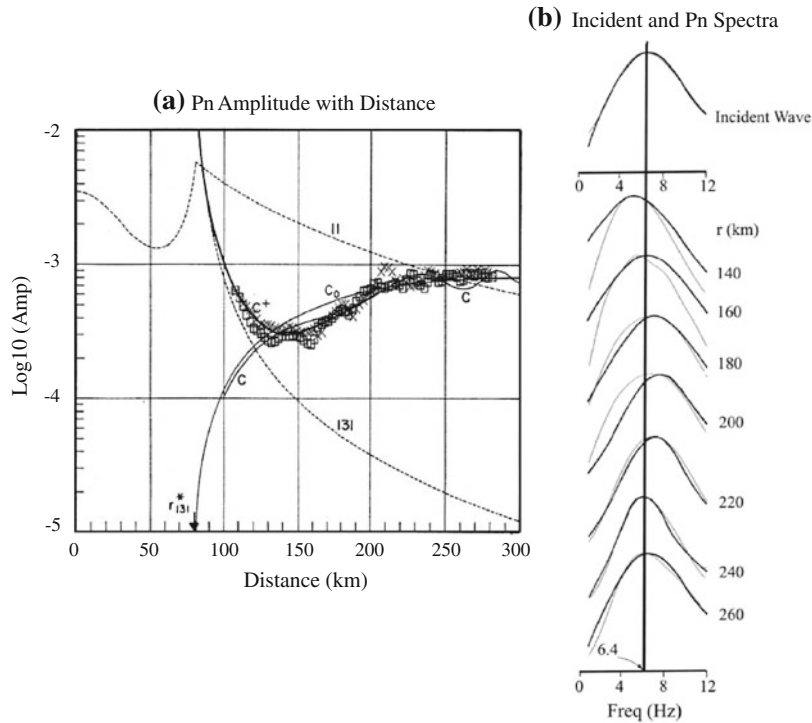


Figure 4

**a** This shows a comparison between the SEM calculations (*crosses* and *squares*) for the random depth models in Fig. 3 and the reference asymptotic results for the interference head-wave (see Fig. 2 for more details of the background plot modified from ČERVENÝ and RAVINDRA, 1971). Crosses are for realization A, and squares are the realization B in Fig. 3. The SEM simulations are corrected from 2D to 3D as in Appendix A. **b** This shows the *Pn* spectra as a function of distance. The *thin black curves* are from ČERVENÝ and RAVINDRA (1971) for the reference case, and the *thin gray lines* show the spectra for the SEM calculations for realization A in Fig. 3

parameters (standard deviation and smoothing length), the other model parameters, including the upper mantle velocity gradient, are the same as that used for interference head-wave case shown in Fig. 2.

The SEM amplitudes for the second of the randomly varying Moho models are given in Fig. 6a, and are compared with the interference head-wave results for the reference model from ČERVENÝ and RAVINDRA (1971). The SEM seismic attributes are corrected from 2D to 3D as in Appendix A. It can be seen that the amplitudes of the two realizations for the second random Moho depth models vary about the background amplitude curves indicating that small interface perturbations affect the amplitudes in a stable fashion. For the same standard deviation and smooth length parameters, the A and B realizations for the second random Moho model have a very similar range of amplitudes about the background

amplitude curve. However, the amplitudes for the second random Moho model in Fig. 6 with a standard deviation of 0.25 km and a horizontal smoothing length of 40 km have amplitudes that vary more strongly but still fluctuate about the background curve than the first model. Figure 6b displays the pulse spectra for the A realizations for the second model showing that the pulse frequencies are stable compared to the background model results for small but somewhat larger perturbations in Moho depth.

#### 4. Effects of Upper-Mantle Velocity Gradients on *Pn* Attributes

To test the effects of upper-mantle velocity gradients on the *Pn* attributes, several models with different velocity gradients are simulated using SEM.

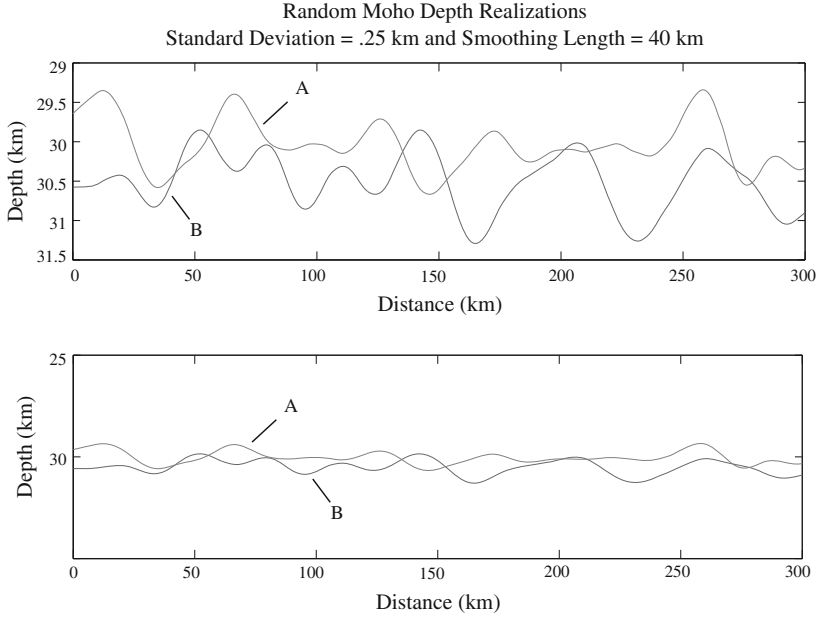


Figure 5

This shows two realizations of random Moho depths A and B for models with a standard deviation of 0.25 km in depth and a horizontal smoothing length of 40 km in distance. The upper mantle velocity gradient is that the same as the used in Fig. 2. Both realizations are centered at 30 km and slightly shifted for plotting purposes. The *top plot* shows a zoomed view of the interfaces, and the *bottom plot* is less magnified

Figure 7a shows the P-wave velocity model for a laterally homogeneous model with an upper-mantle velocity gradient of 0.004 1/s and a Moho depth of 65 km. The crust is laterally homogeneous and has a P-wave velocity of 6 km/s at the surface. Also, a source depth of 10 km was used. Figure 8 shows the SEM  $P_n$  attributes for several models with different upper-mantle velocity gradients of 0, 0.002, 0.004, and 0.006 1/s with and without attenuation included. The incident pulse is a Ricker wavelet with a center frequency of 2 Hz. The SEM simulations are corrected from 2D to 3D as in Appendix A. For positive upper-mantle velocity gradients, it can be seen in Fig. 8a that the travel times as a function of distance curve, with the curvature being most pronounced for the higher velocity gradients. As shown in Fig. 8b, when there is no upper-mantle velocity gradient, the  $P_n$  pulse amplitudes strongly decrease with distance. For the  $P_n$  amplitudes shown in Fig. 8b for the positive upper-mantle velocity gradients in the no attenuation case, the amplitudes even increase for certain distance ranges. In Fig. 8c, the pulse amplitudes are shown with attenuation included for a  $Q_p$  of

150 in the crust and 400 in the mantle, where the attenuation has the effect of bringing down all the amplitude curves in Fig. 8c. Nonetheless, the amplitude patterns are still preserved.

The pulse centroid frequencies shown in Fig. 8d for the no attenuation case initially go down at the intersection of the  $P_g$  and  $P_n$  branches, but then increase higher and even oscillate somewhat with distance for the higher upper-mantle velocity gradients. The pulse centroid frequencies when attenuation is included are shown in Fig. 8e and are now reduced with distance as a result of the attenuation.

### 5. Effects of Large-Scale Lateral Variations on $P_n$ Attributes

SEM simulations are next performed for several models with large-scale, laterally varying structures. Figure 7b shows Ramp Model 1 which is derived from a simplified 2D slice of an earth flattened model derived from the 3D travel time modeling, using regional data from the Hi-CLIMB array from GRIFFIN

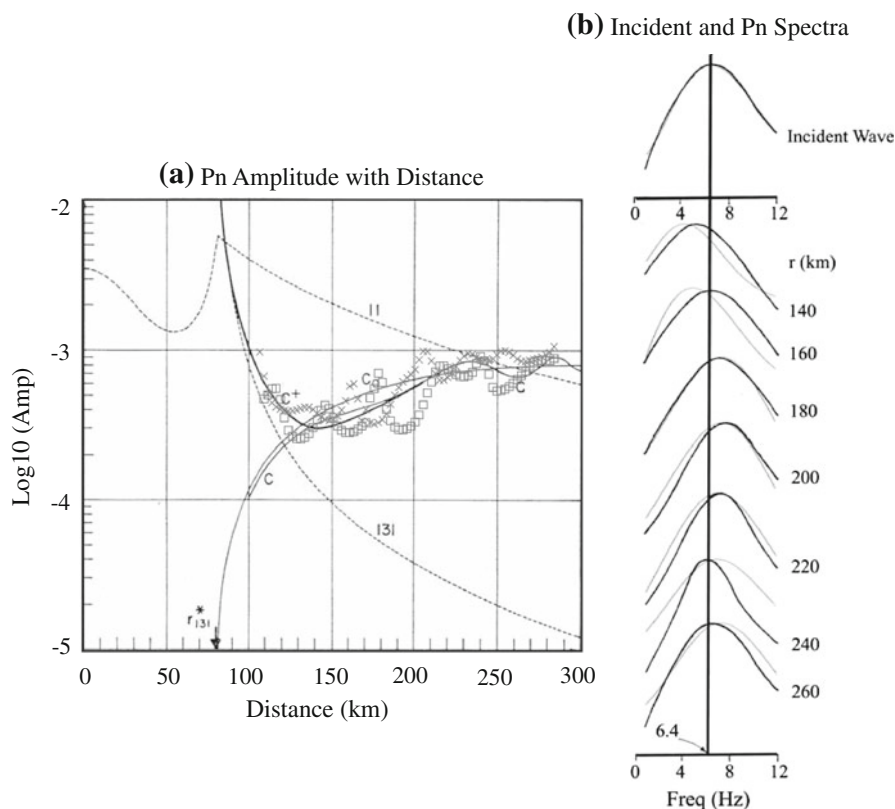


Figure 6

**a** This shows a comparison between the SEM calculations (*crosses* and *squares*) for the Moho depth models in Fig. 5 and the reference asymptotic results for the interference head-wave (see Fig. 2 for more details of the background plot modified from ČERVENÝ and RAVINDRA, 1971). Crosses are for realization A, and squares are for realization B in Fig. 5. The SEM simulations are corrected from 2D to 3D as in Appendix A. **b** This shows the *Pn* spectra as a function of distance. The *black curves* are from ČERVENÝ and RAVINDRA (1971) for the reference case, and the *thin gray curves* shows the spectra for the SEM calculations as a function of distance for realization A in Fig. 5

*et al.* (2011) and using teleseismic waves recorded by the Hi-CLIMB array by NÁBĚLEK *et al.* (2009), NOWACK *et al.* (2010) and TSENG *et al.* (2009). The laterally homogeneous crust has a velocity of 6 km/s at the surface. The upper-mantle has velocity gradients with depth and also velocities that can change laterally. The Moho has a ramp structure with the Moho changing in depth from 73 km on the left side of the ramp to 64 km on the right side of the ramp. The upper-mantle top velocities are 8.3 km/s to the left of the ramp and 7.9 km/s to the right of the ramp with a linear transition in between. Ramp Model 1 has a constant upper-mantle velocity gradient of 0.004 1/s. Figure 7c shows Ramp Model 2 which is similar to Ramp Model 1 but with a laterally variable upper-mantle velocity gradient with 0.004 1/s to the

left of the ramp and 0.002 1/s to the right of the ramp. The source depth is 10 km.

Figure 9 shows the seismic attributes computed for Ramp Model 1. The crosses are for source B near 1,000 km and recorded to the left in Fig. 7b and the circles are for source A near 0 km and recorded to the right in Fig. 7b. The travel time curves are shown in Fig. 9a and are quite distinct between the normal and reversed gathers from shots A and B, and this results from the different upper-mantle top velocities to the left and right of the ramp, as well as the change of Moho depth structure across the model. The amplitudes curves are displayed in Fig. 9b for the no attenuation case and show a relative increase with distance for the *Pn* branch for source B which results from the ramp in the Moho

## Modeling Seismic Attributes of $P_n$ Waves

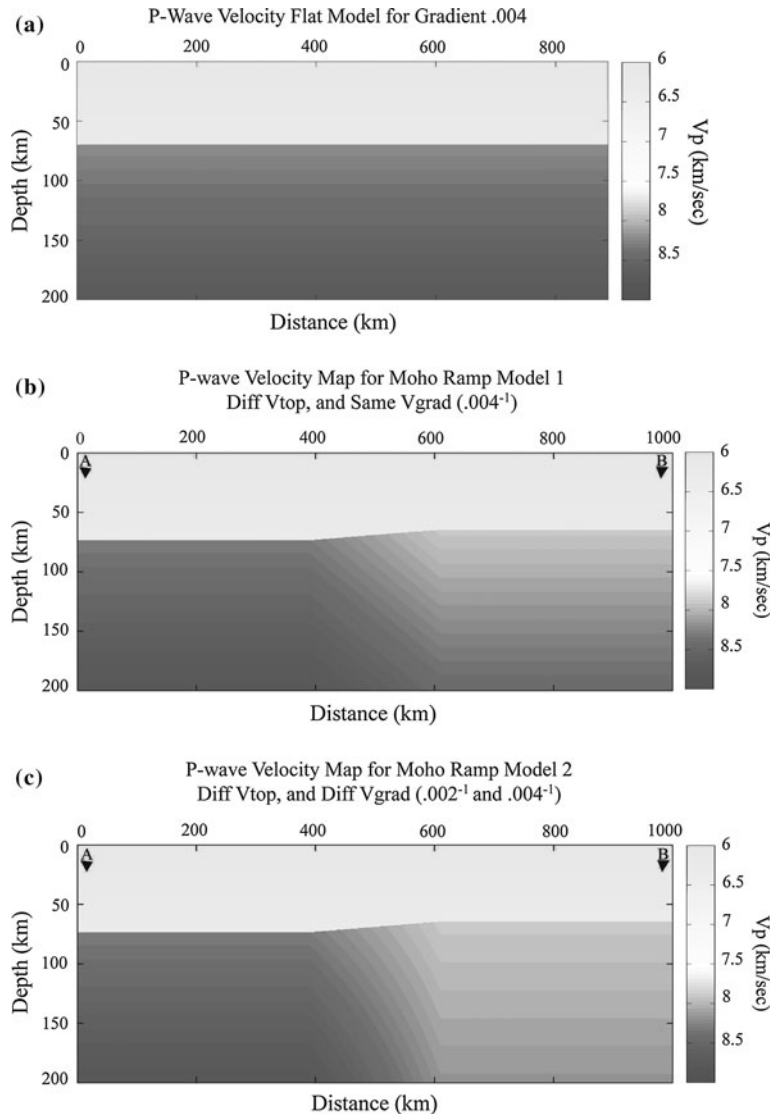


Figure 7

**a** This shows a horizontal Moho structure with a positive velocity gradient of 0.004 1/s in the upper-mantle. **b** This shows Ramp Model 1, a simplified P-wave velocity model from travel time modeling of regional events from Hi-CLIMB, showing a ramp in the Moho with a constant velocity gradient of 0.004 1/s in the mantle. **c** This shows Ramp Model 2, a ramp model with an upper-mantle velocity gradient of 0.004 1/s on the left side of the ramp and 0.002 1/s on the right side of the ramp. The Moho is at a depth of 73 km on the left side of the ramp and 64 km on the right side. The top velocity of the upper-mantle is 8.3 km/s on the left side of the ramp and 7.9 km/s on the right side. The normal and reversed shot gathers have shots located at A and B

for this model. However, for source A, the  $P_n$  amplitudes relatively decrease with distance, resulting from the ramp in the Moho. Figure 9c shows the amplitudes for the Ramp Model 1 when attenuation is included with a  $Q_p$  of 150 in the crust, and 400 in the mantle. When attenuation is included, the

amplitudes are brought down with distance but have a similar pattern as in the no attenuation case. Nonetheless, using reversed shot gathers to the left and right of the model, one can identify the large-scale features of the ramp and upper-mantle velocity structure for this model.

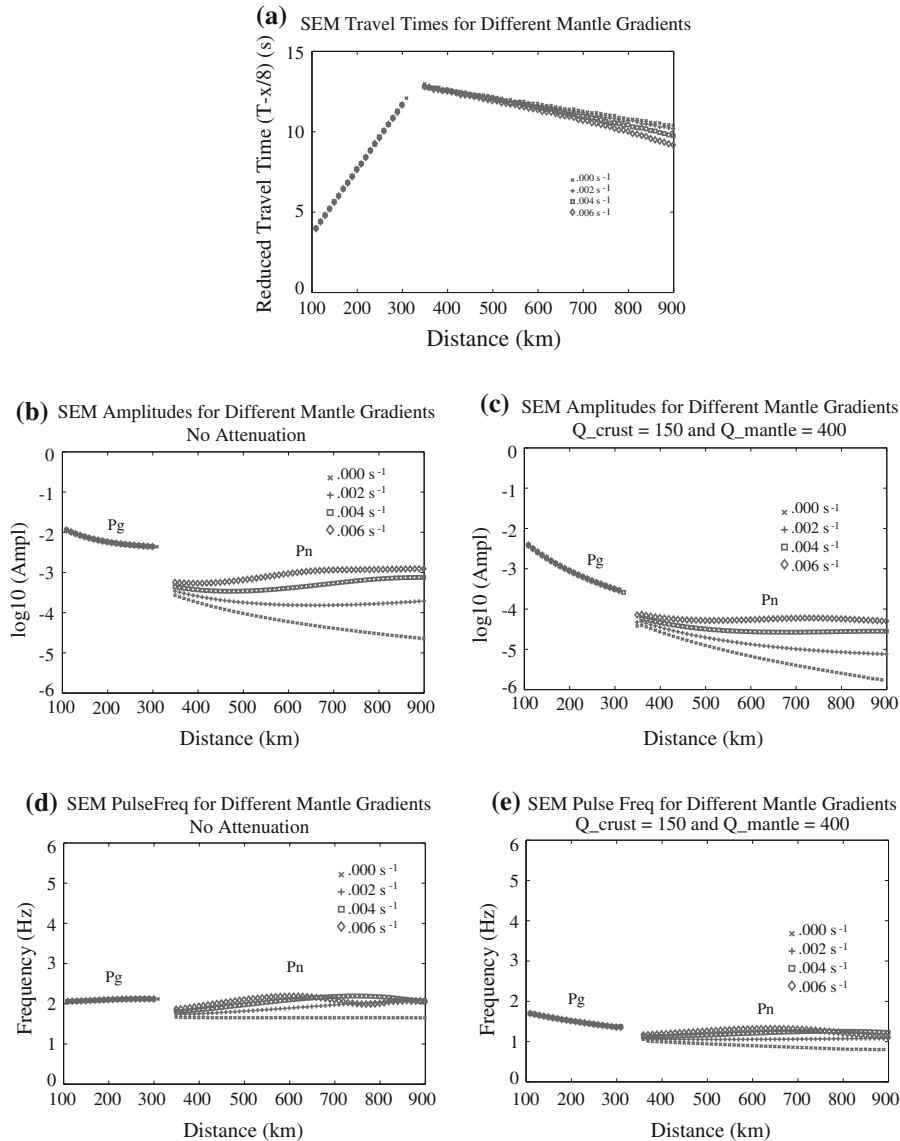


Figure 8

This shows the SEM seismic attributes for the horizontal Moho model shown in Fig. 7a with different upper-mantle velocity gradients of 0.0, 0.002, 0.004 and 0.006 1/s. **a** The travel times. **b** The amplitudes with no attenuation. **c** The amplitudes for a model with attenuation included with a  $Q_p$  of 150 in the crust and 400 in the mantle. The SEM simulations are corrected from 2D to 3D as in Appendix A. **d** The pulse frequencies with no attenuation. **e** The pulse frequencies with attenuation included as in **c**

The pulse frequencies for the no attenuation case are displayed in Fig. 9d, but the structure shows a less dramatic difference between the normal and reverse shot gathers. The pulse frequencies for the attenuation case are shown in Fig. 9e and the effects of the ramp structure are more subdued than in the no attenuation case. However, the *Pn* pulse frequencies

still show a slight increase with distance resulting from the upper-mantle velocity gradient.

Ramp Model 2 is shown in Fig. 7c and has the same ramp structure and upper-mantle top velocities as Ramp Model 1. However, Ramp Model 2 has a laterally varying upper mantle velocity gradient, where to the left of the ramp the upper-mantle

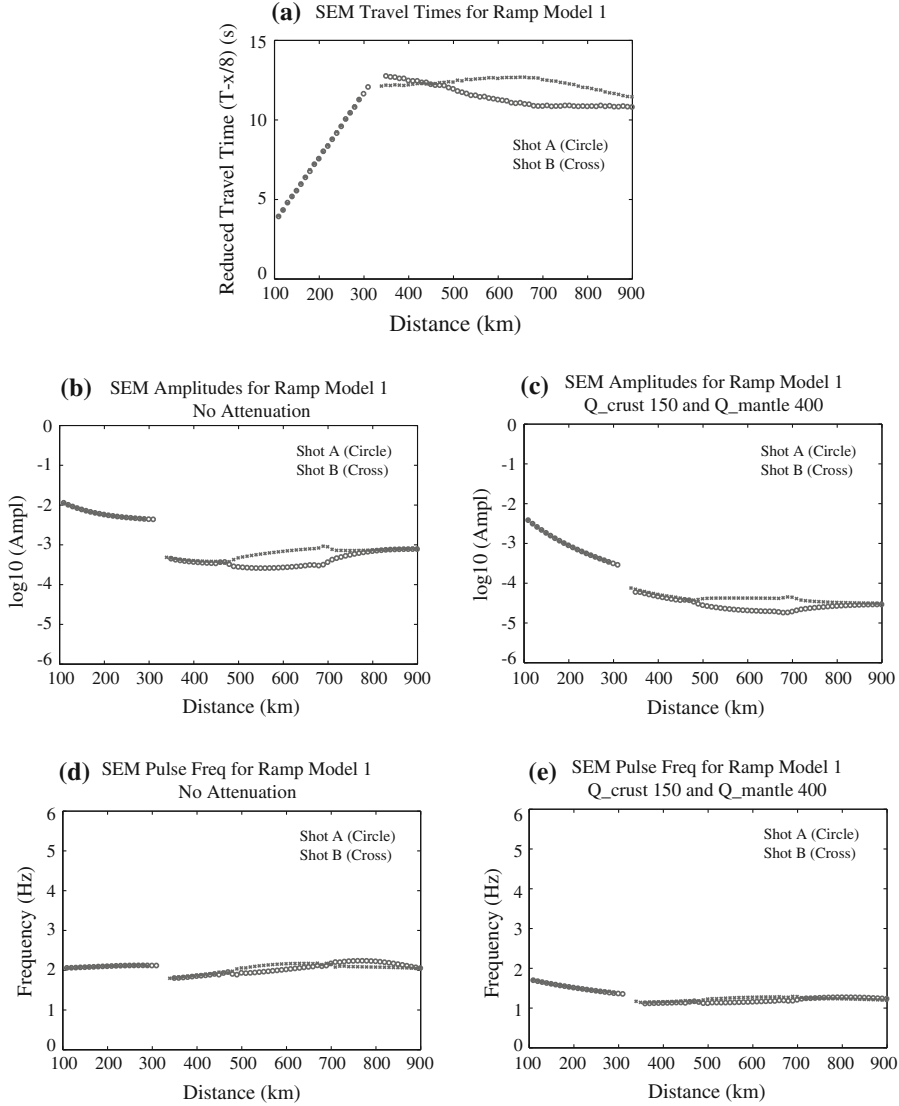


Figure 9

This shows the SEM seismic attributes for Ramp Model 1 shown in Fig. 7b with a constant upper-mantle velocity gradient of 0.004 1/s. **a** The travel times. **b** The amplitudes with no attenuation. **c** The amplitudes with attenuation included with a  $Q_p$  of 150 in the crust and a  $Q_p$  of 400 in the mantle. The SEM simulations are corrected from 2D to 3D as in Appendix A. **d** The pulse frequencies with no attenuation. **e** The pulse frequencies with attenuation. The crosses are for a source B near 1,000 km in Fig. 7b and recorded to the south, and the circles are for a source A near 0 km and recorded to the north

velocity gradient is 0.004 1/s and to the right of the ramp the upper-mantle velocity gradient is 0.002 1/s. The travel times are shown in Fig. 10a for the reversed shots A and B and the difference in the slopes of the travel time curves primarily result from the change of top velocities in the upper-mantle across the model, as well as the change of Moho depth. The amplitudes for the no attenuation case are

shown in Fig. 10b, where the amplitudes for shot A are almost balanced with those from shot B. For the shot A gather (from left to the right), the thinning crust to the right increases the amplitudes with distance, while a lower velocity gradient lowers the amplitudes and balances the with the effect of the ramp. For the shot B gather (from right to the left), the thickening crust decreases the amplitudes with

distance, while the higher velocity gradient in the upper-mantle to the left increases the amplitudes, again balancing with the effect of the ramp. As a result, the amplitudes from shots A and B are also approximately balanced from the competing effects of Moho structure and upper-mantle velocity gradients.

Figure 10c shows the amplitudes for Ramp Model 2 for the attenuation case with a  $Q_p$  of 150 in the crust and a  $Q_p$  of 400 in the mantle. The attenuation is seen to bring down the amplitudes but keep the relative patterns between the normal and reversed shots the same. Figure 10d shows the pulse frequencies for the no attenuation case and again there is a balancing

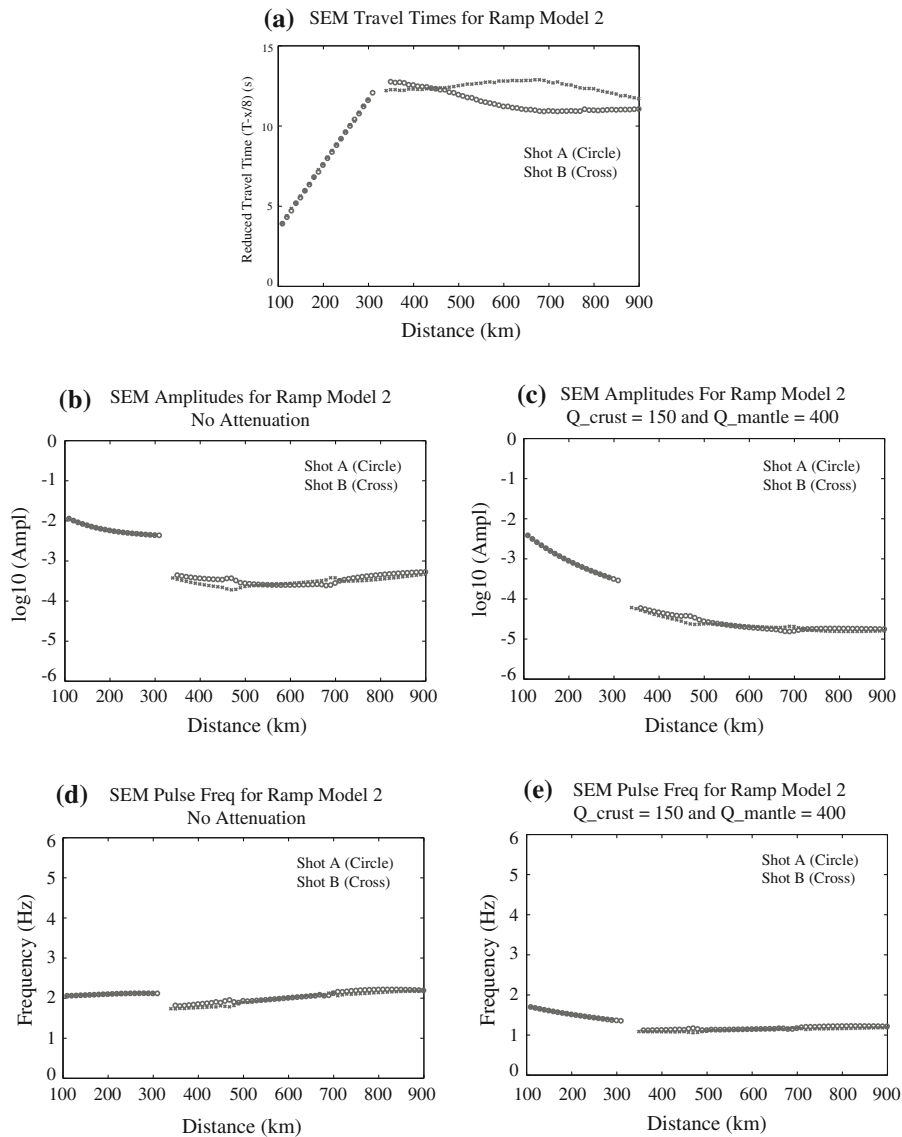


Figure 10

This shows the SEM seismic attributes for Ramp Model 2 shown in Fig. 7c with a constant upper-mantle velocity gradient of 0.004 1/s on the left side of the ramp and 0.002 1/s on the right side. **a** The travel times. **b** The amplitudes with no attenuation. **c** The amplitudes with attenuation included with a  $Q_p$  of 150 in the crust and a  $Q_p$  of 400 in the mantle. The SEM simulations are corrected from 2D to 3D as in Appendix A. **d** The pulse frequencies with no attenuation. **e** The pulse frequencies with attenuation. The crosses are for a source B near 1,000 km in Fig. 7c and recorded to the south, and the circles are for a source A near 0 km and recorded to the north in Fig. 7c

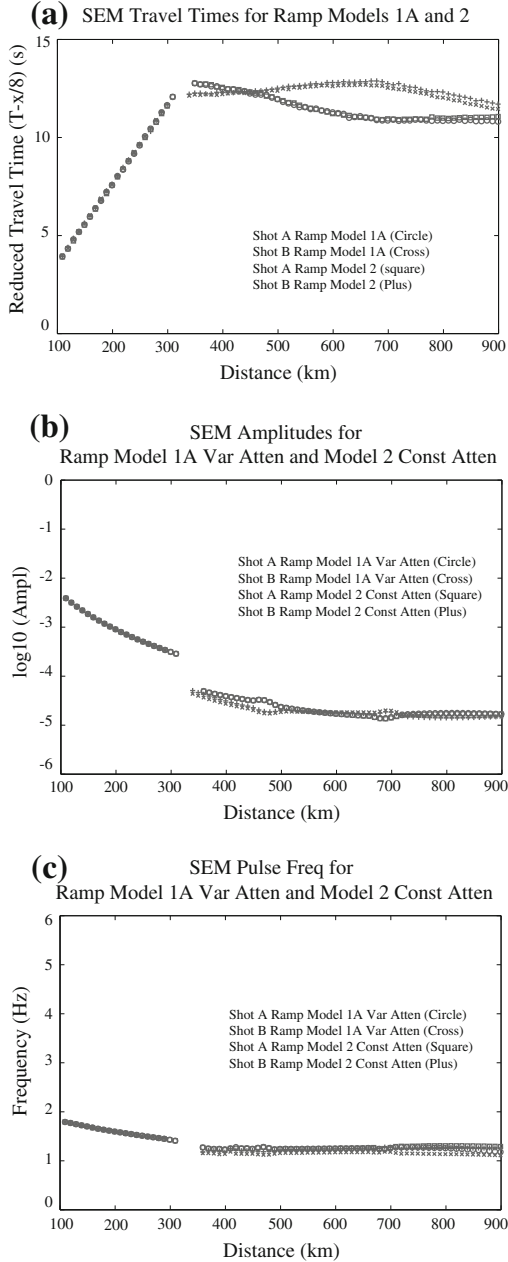


Figure 11

This shows a comparison of the SEM seismic attributes of the modified Ramp Model 1A with a variable attenuation with a  $Q_p$  of 400 to the left of the ramp and 200 to the right of the ramp in the upper-mantle, and Ramp Model 2 with a variable upper-mantle velocity gradient as in Fig. 10 and a constant  $Q_p$  of 400 in the upper mantle. **a** The travel times. **b** The amplitudes. The SEM simulations are corrected from 2D to 3D as in Appendix A. **c** The pulse frequencies. The circles are for shot A and the crosses are for shot B for Ramp Model 1A, and the squares are for Shot A and the plus signs for Shot B for Ramp Model 2

from the effects of the different upper-mantle and Moho structures. The pulse frequencies are shown in Fig. 10e for the attenuation case, and are seen to bring down the pulse frequencies relative to the no attenuation case, but a slight increase with distance is still seen.

A final test is shown in Fig. 11 where Ramp Model 2 with a laterally varying upper-mantle velocity gradient and a constant attenuation is compared with a modified Ramp Model 1, called Ramp Model 1A, now using a laterally varying attenuation model with a  $Q_p$  of 400 in the mantle to the left of the ramp and a  $Q_p$  of 200 to the right of the ramp. Figure 11a shows a comparison of the travel times for the forward and reversed gathers from shots A and B for the two cases. The change of upper-mantle velocity gradients can begin to be observed in the travel times at distance ranges larger than about 700 km. This effect is less than that shown in Fig. 8 since the upper-mantle velocity gradient is now changed for only half the model. But the dominant effect on the travel time is still the Moho structure and upper-mantle top velocities for these models and distance ranges. The amplitudes are shown in Fig. 11b, and are seen to be balanced both for the forward and reversed shots A and B, and also for the Ramp Models 1A and 2. For the case of Ramp Model 1A the change in upper-mantle attenuation is now compensating for the change in Moho depth in the amplitudes. For Ramp Model 2, the change in upper-mantle velocity gradient is balancing the change in Moho depth. In Fig. 11c, these compensating effects are also seen for the pulse frequencies. Thus, for these models and distance ranges, there is a trade-off between these models with respect to the  $P_n$  amplitude and frequency attributes. However, at larger offsets the travel times might be used to distinguish these alternative models, but longer offsets than used here would be needed.

## 6. Discussion and Conclusions

In this study, we have implemented the 2D spectral-element method (SEM) to investigate  $P_n$  propagation for vertically and laterally varying media

with and without attenuation. As a practical measure, essential features of the  $Pn$  waves have been distilled into seismic attributes, including arrival times, amplitudes and pulse frequencies as described by MATHENEY and NOWACK (1995). To validate the SEM simulations, we compared the SEM simulations with reflectivity calculations of BRAILE and SMITH (1975) and with the asymptotic results of ČERVENÝ and RAVINDRA (1971). After the source time functions between the different methods were matched and an approximate 2D to 3D correction was applied to the 2D SEM results, good agreement was found with the other methods. In the future, we will implement the full 3D SEM which will increase the accuracy of the simulations in laterally varying models, as well as allowing for more realistic surface topography, basin geometry, Moho topography, and 3D wave speed heterogeneity (LEE *et al.*, 2008). Also, certain phenomena cannot be properly simulated by 2D methods, including 3D forward scattering/multipathing, accurate out-of-plane spreading and 3D finite frequency effects. But complete 3D SEM simulations will involve substantially more computational time, even on a parallel computer cluster, compared to the 2D SEM simulations for the frequency ranges that we have investigated here.

Models with random, laterally varying Moho structures were then simulated, where the amplitude and pulse frequency characteristics were found to be stable with regard to small Moho interface perturbations. However, larger random depth variations affected the seismic attributes more strongly. This was also found by AVANTS *et al.* (2011) for random Moho depth variations. In addition, they also showed that lateral variations of upper-mantle velocity gradients can affect the  $Pn$  amplitudes more strongly than random variations of Moho depths. This can be understood by the fact that random variations of the upper-mantle velocity gradients can disrupt the formation of the gallery effects for the interference head-waves. However, MOROZOV *et al.* (1998) successfully modeled observed  $Pn$  data from the Quartz profile in Russia in terms of the whispering gallery effect of the interference head-wave, along with the incoherent  $Pn$  coda being modeled by random velocity variations in the crust. NIELSEN and THYBO (2003) also modeled observed  $Pn$  as upper-mantle

whispering gallery phases with the  $Pn$  coda resulting from random crustal velocity variations. Thus, the effects of random velocity variations may be more dominant in the crust and from lateral variations in the Moho depth than from random velocity variations in the upper-mantle.

Nonetheless, the magnitude of the upper-mantle velocity gradient for a given region can strongly affect the seismic attributes of the  $Pn$  wave. YANG *et al.* (2007) also modeled the interference head-wave from an effective upper-mantle velocity gradient from the earth flattening of a spherical Earth. Here we used SEM simulation to model the effects of different upper-mantle velocity gradients on the  $Pn$  seismic attributes. When attenuation is not included, the  $Pn$  amplitudes can even increase with distance as the diving wave begins to dominate. Pulse frequencies of the  $Pn$  wave can also increase with distance resulting from a tuning effect of the whispering gallery wave propagating beneath the Moho (NOWACK and STACY, 2002). However, the addition of attenuation will generally reduce the  $Pn$  amplitudes and pulse frequencies in comparison to the no attenuation case.

For larger scale laterally varying structures, SEM simulations are then performed for earth flattened models similar to those found along the Hi-CLIMB array in Tibet by GRIFFIN *et al.* (2011) using the modeling of regional travel times and NÁBĚLEK *et al.* (2009), NOWACK *et al.* (2010) and TSENG *et al.* (2009) using teleseismic waves. Performing SEM simulations here, it was found that large scale structure can significantly affect  $Pn$  seismic attributes. The sensitivity of  $Pn$  seismic attributes to laterally varying velocity structure has both advantages and disadvantages. An advantage is that this high sensitivity allows for the possibility of inverting  $Pn$  attributes for structure. A disadvantage is that accounting for the propagation effects of  $Pn$  waves for source studies requires a detailed knowledge of the Moho and upper mantle velocity structure.

Although GRIFFIN *et al.* (2011) modeled the regional travel times using laterally varying upper-mantle top velocities, they used a constant upper-mantle velocity gradient for central Tibet that was found by PHILLIPS *et al.* (2007). In contrast, MYERS *et al.* (2010), while performing a large regional study for Eurasia and North Africa, found different upper-

mantle velocity gradients between southern and central Tibet. However, they also found different upper-mantle top velocities in central Tibet than were found from more detailed regional studies in Tibet (e.g. LIANG and SONG, 2006; GRIFFIN *et al.* 2011). Using SEM simulations here, we found that there can be ambiguities between upper-mantle velocity gradients and attenuation when using  $Pn$  amplitudes and pulse frequency attributes. These ambiguities may be resolved, to some degree, by using the curvature of  $Pn$  travel times at longer regional distance, however, this would also be complicated by lateral variability.

### Acknowledgments

This work was supported by the U.S. National Science Foundation grant EAR06-35611, and the Air Force Research Laboratory contract FA8718-08-C-002.

### Appendix A

To compare the SEM results with reflectivity, the pulse shapes of the initial sources for each method need to be the same. In the reflectivity calculations of BRAILE and SMITH (1975), the source time function is given by

$$s(t) = \sin(\delta t) - \frac{1}{m} \sin(m\delta t) \text{ where } 0 \leq t \leq \tau, \quad (1)$$

where

$$\delta = \frac{N\pi}{\tau}, \quad m = \frac{N+2}{N}, \quad (2)$$

and  $N$  is an integer used to define the number of extrema of the pulses and is the duration of the source wavelet, where  $N = 2$  and  $\tau = 0.2\text{s}$  are used by BRAILE and SMITH (1975). In the SEM modeling, the first derivative of a Gaussian distribution is chosen to provide a similar source pulse shape as the reflectivity modeling. The initial source time function in the SEM calculations is given by

$$s(t) = -2A(\pi^2 a_0^2) e^{-\pi^2 a_0^2 (t-t_0)^2} \quad (3)$$

where  $A$  is a multiplication factor,  $a_0$  is related to the width of the source time function, and  $t_0$  is the time

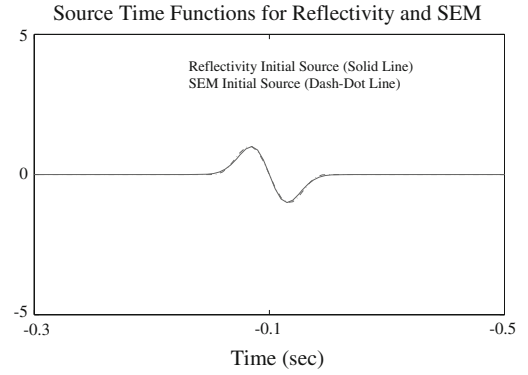


Figure 12  
Source time functions for the reflectivity (*solid line*) and the SEM calculations (*dash-dot line*)

delay. In order to make the pulses similar,  $a_0 = 7.4$  is found to be appropriate for the SEM source time function as shown in Fig. 12.

Seismic amplitudes vary in a different manner for 2D and 3D wave waves (CHEW, 1990). Since the reflectivity results from BRAILE and SMITH (1975) are calculated for 3D, while SEM calculations are for 2D, the amplitude variations with distance will be different. In the 2D SEM, the source can be considered a line source, where  $R$  is the distance from the source,  $U(x, y) = U(R)$  and  $\delta(x)\delta(y) = \delta(R)$ . Assuming that has a time dependence  $e^{-i\omega t}$ , the homogeneous wavefield can be written as

$$U(R) \sim \frac{1}{4} \sqrt{\frac{2\alpha}{\pi\omega R}} e^{i\pi/4} e^{i\omega R/\alpha} \quad (4)$$

where  $\omega$  is the radial frequency and  $\alpha$  is the wave speed. For the 3D reflectivity method, the source is a point source where the homogeneous wavefield can be written as

$$U(R) = \frac{1}{4\pi R} e^{i\omega R/\alpha}. \quad (5)$$

To compare the 2D SEM amplitudes with the 3D reflectivity results, the 2D SEM results can be approximately multiplied by

$$\frac{1}{\pi} \sqrt{\frac{\pi\omega}{2\alpha R}} e^{-i\pi/4}. \quad (6)$$

SEM synthetics for model Moho-1, before and after 2D to 3D correction are shown in Fig. 13.

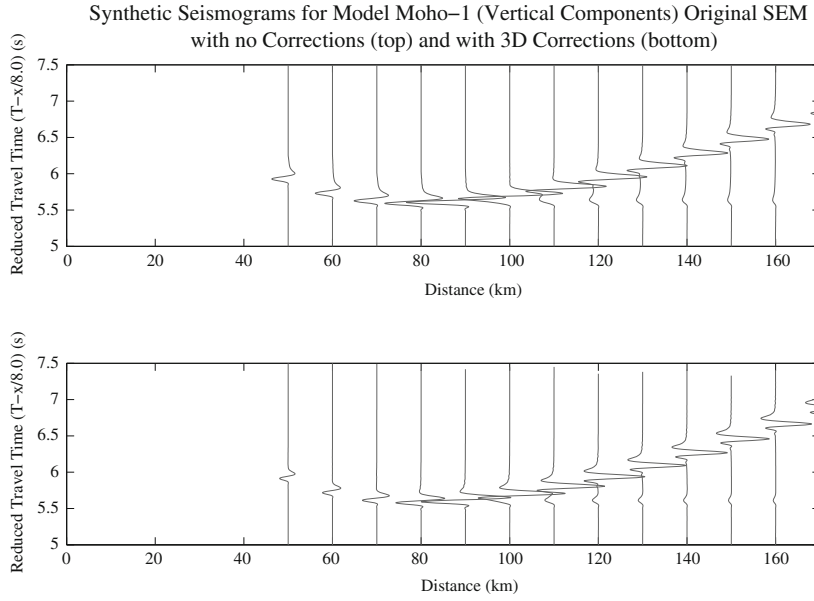


Figure 13

SEM synthetics for model Moho-1 with no 3D correction (*top*) and with 3D distance and pulse shape corrections (*bottom*)

Although this correction is only for a homogeneous media, it can still be approximately applied for the wide-angle  $Pn$  wavefield for out-of-plane spreading for a medium varying only in the 2D plane, where now  $R$  is the horizontal range. Higher order asymptotic corrections for 2D to 3D are given by MIKSAT *et al.* (2008), as well as by VIDALE *et al.* (1985), HELMBERGER and VIDALE (1988).

### Appendix B

In this appendix, the SEM calculations including attenuation are compared with the analytical solution. The effect of a constant  $Q$  attenuation on the wavefield can be written (AKI and RICHARDS, 2002) as

$$U(R, \omega) = U_0(\omega) e^{-\frac{\omega R}{2\alpha Q}} \quad (7)$$

where  $\omega$  is the radial frequency,  $R$  is the distance,  $\alpha$  is the velocity of the medium,  $Q$  is the quality factor of the medium, and  $U(R, \omega)$  is the attenuated wavefield. To test the effect of attenuation on the SEM wavefield, a homogeneous model with a  $Q_p$  of 112.5, a P-wave velocity of 5 km/s, and a dominant frequency

of 2 Hz is used to calculate the wavefield for different source-receiver distances.

For this test, a receiver is put at the surface and four shots at different depths vertically below the receiver are used to calculate the SEM synthetics. The SEM calculations in the frequency domain are then compared with a constant  $Q$  filter applied to the near offset SEM trace at 10 km depth.  $Q_p$  can be written in terms of the bulk and shear  $Q_\kappa$  and  $Q_\mu$  as

$$\frac{1}{Q_p} = \left(1 - \frac{4\beta^2}{3\alpha^2}\right) \frac{1}{Q_\kappa} + \frac{4}{3} \left(\frac{\beta^2}{\alpha^2}\right) \frac{1}{Q_\mu} \quad (8)$$

where  $\alpha$  and  $\beta$  are the P and S wave velocities of the media and  $Q_\mu$  is equal to  $Q_s$  (DAHLEN and TROMP, 1998). The bulk attenuation is neglected by choosing a large  $Q_\kappa$  and for a Poisson solid  $Q_p = (9/4) Q_s$ . For this test  $Q_s$  is chosen as 50 resulting in a  $Q_p$  of 112.5 from the ratio of  $Q_p = (9/4) Q_s$  for a large  $Q_\kappa$ . In order to retain this ratio between  $Q_p$  and  $Q_s$ , all SEM calculations in the paper are made based on assuming attenuation loss in shear. Figure 14 shows the spectral comparisons of the original SEM traces with the analytically calculated traces where a good agreement is obtained.

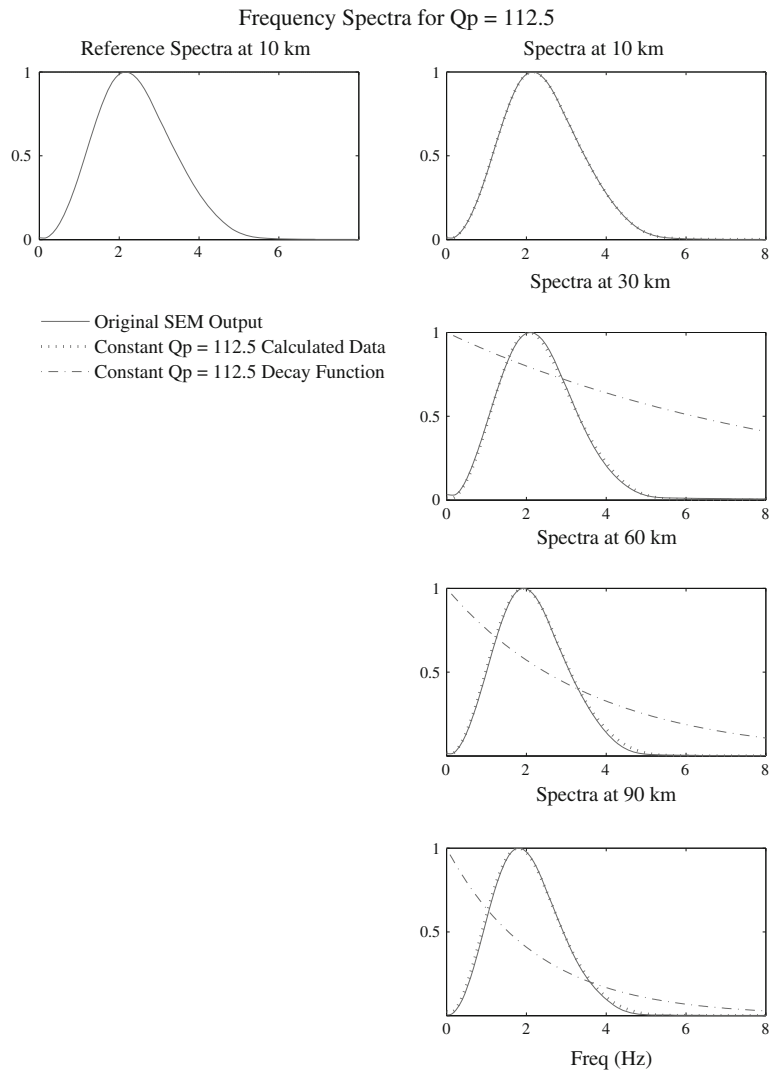


Figure 14

This the frequency spectra of the SEM traces for a  $Q_p$  of 112.5 compared with the analytical calculations for the same  $Q_p$

### Data and Resources

The spectral-element method (SEM) was performed using the SPECFEM2D code by KOMATITSCH and VILOTTE (1998) and KOMATITSCH *et al.*, (2005).

### REFERENCES

AKI, K., and RICHARDS, P.G. (2002) *Quantitative Seismology*. University Science Books.

AVANTS, M., LAY, T., XIE, X.B., and YANG, X. (2011). *Effects of 2D random velocity heterogeneities in the mantle lid and Moho topography on  $P_n$  geometric spreading*. Bull. Seism. Soc. Am. *101*, 126–140.

BRAILE, L.W., and SMITH, R.B. (1975). *Guide to the interpretation of crustal refraction profiles*. Geophys. J.R. Astr. Soc. *40*, 145–176.

ČERVENÝ, V., and RAVINDRA, R. (1971). *Theory of Seismic Head Waves*. University of Toronto Press, pp. 235–250.

CHEW, W.C. (1990). *Waves and Fields in Inhomogeneous Media*. Nostrand Reinhold Book Co., pp. 57–66.

DAHLEN, F.A., TROMP, J. (1998). *Theoretical Global Seismology*. Princeton University Press, pp. 327–350.

GRIFFIN, J.D., NOWACK, R.L., CHEN, W. P. and TSENG, T. L. (2011). *Velocity structure of the Tibetan lithosphere: Constraints from*

- P-wave travel times of regional earthquakes.* Bull. Seism. Soc. Am. 101, 1938–1947.
- HELMBERGER, D., and VIDALE, J.E. (1988). *Modeling strong motions produced by earthquakes with two-dimensional numerical codes.* Bull. Seism. Soc. Am. 78, 109–121.
- HILL, D.P. (1971). *Velocity gradients and anelasticity from crustal body wave amplitudes.* J. Geophys. Res. 76, 3309–3325.
- HILL, D. P. (1973). *Critically refracted waves in a spherical symmetric radially heterogeneous earth model.* Geophys. J. R. Astr. Soc. 34, 149–177.
- KOMATITSCH, D., VILOTTE, J.P. (1998). *The spectral elements method: An efficient tool to simulate the seismic response of 2D and 3D geological structure.* Bull. Seism. Soc. Am. 88, 368–392.
- KOMATITSCH, D., TSUBOI, S., TROMP, J. (2005). The spectral element method in seismology, in *Seismic Earth: Array Analysis of Broadband Seismograms*, ed by LEVANDER A., and NOLET, G. American Geophysical Union Monograph 157, pp. 205–227.
- LEE, S.-J., CHEN, H.-W., LIU, Q., KOMATITSCH, D., HUANG, B.-S., and TROMP, J. (2008). *Three-dimensional simulations of seismic-wave propagation in the Taipei basin with realistic tomography based upon the spectral-element method.* Bull. Seism. Soc. Am. 98, 253–264.
- LIANG, C., and SONG, X. (2006). *A low velocity belt beneath northern and eastern Tibetan Plateau from Pn tomography.* Geophys. Res. Lett. 33, L22306.
- MATHENEY, M.P., and NOWACK, R.L. (1995). *Inversion of seismic attributes for velocity and attenuation.* Geophys. J. Int. 128, 689–700.
- MENKE, W. H., RICHARDS, P.G. (1980). *Crust-mantle whispering gallery phases: A deterministic model of teleseismic Pn wave propagation.* J. Geophys. Res. 85, 5416–5422.
- MIKSAT, J., MULLER, T.M., and WENZEL, F. (2008). *Simulating three-dimensional seismograms in 2.5-dimensional structures by combining two-dimensional finite difference modeling and ray tracing.* Geophys. J. Int. 174, 309–315.
- MOROZOV, I.B. (2008). *Geometrical attenuation, frequency dependence of Q, and the absorption band problem.* Geophys. J. Int. 175, 239–252.
- MOROZOV, I.B. (2010). *On the causes of frequency-dependent apparent seismological Q.* Pure Appl. Geophys. 167, 1131–1146.
- MOROZOV, I. B., MOROZOVA, E. A., SMITHSON, S. B., SOLODILOV, L. N. (1998). *On the nature of teleseismic Pn phase observed on the ultralong-range profile “Quartz”, Russia.* Bull. Seism. Soc. Am. 88, 62–73.
- MYERS, S. C., BEGNAUD, M. L., BALLARD, S., PASYANOS, M. E., PHILLIPS, W. S., RAMIREZ, A. L., ANTOLIK, M. S., HUTCHENSON, K. D., DWYER, J. J., ROWE, C. A., WAGNER G. S. (2010). *A crust and upper-mantle model of Eurasia and North Africa for Pn travel time calculation.* Bull. Seism. Soc. Am. 100, 640–656.
- NÁBĚLEK, J., HETÉNYI, G., VERGNE, J., SAPKOTA, S., KAFLE, B., JIAN, M., SU, H., CHEN, J., HUANG, B.S. (2009). *Underplating in the Himalaya-Tibet Collision Zone Revealed by the Hi-CLIMB Experiment.* Science 325, 1371–1374.
- NIELSEN, L., THYBO, H. (2003). *The origin of teleseismic Pn waves: Multiple crustal scattering of upper mantle whispering gallery phases.* J. Geophys. Res. 108, B10, Article No. 2460.
- NOWACK, R. L., STACY, S. M. (2002). *Synthetic seismograms and wide-angle seismic attributes from the Gaussian Beam and Reflectivity methods for models with interfaces and velocity gradients.* Pure Appl. Geophys. 159, 1447–1464.
- NOWACK, R.L., CHEN, W. P., TSENG, T. L. (2010). *Application of Gaussian Beam Migration to Multi-Scale Imaging of the Lithosphere Beneath the Hi-CLIMB Array in Tibet.* Bull. Seism. Soc. Am. 100, 1743–1754.
- SERENO, T. J., GIVEN, J.W. (1990). *Pn attenuation for a spherically symmetric earth model.* Geophys. Res. Lett. 17, 1141–1144.
- PHILLIPS, W.S., BEGNAUD, M.L., ROWE, C.A., STECK, L.K., MYERS, S.C., PASYANOS, M.E., and BALLARD, S. (2007). *Accounting for lateral variations of the upper mantle gradient in Pn tomography studies.* Geophys. Res. Lett. 34, L14312.
- TSENG, T.-L., CHEN, W.P., NOWACK, R.L. (2009). *Northward thinning of Tibetan crust revealed by virtual seismic profiles.* Geophys. Res. Lett. 36, L24304.
- VIDALE, J., HELMBERGER, D.V., and CLAYTON, R.W. (1985). *Finite-difference seismograms for SH waves.* Bull. Seism. Soc. Am. 75, 1765–1782.
- XIE, J. (2010). *Can we improve estimates of seismological Q using a new “geometrical spreading” model?* Pure Appl. Geophys. 167, 1147–1162.
- YANG, X., LAY, T., XIE, X., and THORNE, M.S. (2007). *Geometric spreading of Pn and Sn in a spherical Earth model.* Bull. Seism. Soc. Am. 97, 2053–2065.